Article

Interface Dynamics in Ag−Cu$_3$P Nanoparticle Heterostructures

Michael S. Seifner,* Markus Snellman, Ofentse A. Makgae, Krishna Kumar, Daniel Jacobsson, Martin Ek, Knut Deppert, Maria E. Messing, and Kimberly A. Dick*

ACCESS | Metrics & More | Article Recommendations | SI Supporting Information

ABSTRACT: Earth-abundant transition metal phosphides are promising materials for energy-related applications. Specifically, copper(I) phosphide is such a material and shows excellent photocatalytic activity. Currently, there are substantial research efforts to synthesize well-defined metal−semiconductor nanoparticle heterostructures to enhance the photocatalytic performance by an efficient separation of charge carriers. The involved crystal facets and heterointerfaces have a major impact on the efficiency of a heterostructured photocatalyst, which points out the importance of synthesizing potential photocatalysts in a controlled manner and characterizing their structural and morphological properties in detail. In this study, we investigated the interface dynamics occurring around the synthesis of Ag−Cu$_3$P nanoparticle heterostructures by a chemical

reaction between Ag−Cu nanoparticle heterostructures and phosphine in an environmental transmission electron microscope. The major product of the Cu−Cu$_3$P phase transformation using Ag−Cu nanoparticle heterostructures with a defined interface as a template preserved the initially present Ag{111} facet of the heterointerface. After the complete transformation, corner truncation of the faceted Cu$_3$P phase led to a physical transformation of the nanoparticle heterostructure. In some cases, the structural rearrangement toward an energetically more favorable heterointerface has been observed and analyzed in detail at the atomic level. The herein-reported results will help better understand dynamic processes in Ag−Cu$_3$P nanoparticle heterostructures and enable facet-engineered surface and heterointerface design to tailor their physical properties.
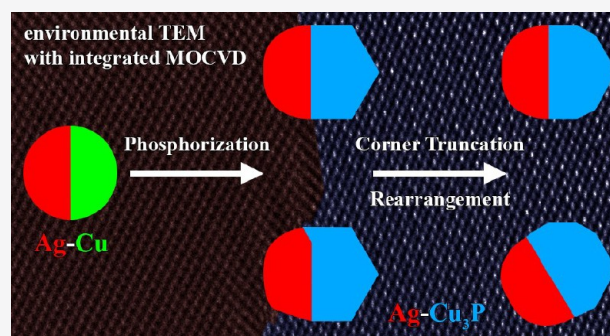
INTRODUCTION

Over the last years, nanostructured transition metal phosphides (TMPs) have been the focus of several research efforts due to their excellent performance in energy-related applications, including electrocatalysis, photocatalysis, and energy storage.[1] Most of the targeted TMPs with high potential in this research field are earth-abundant and could become a cost-efficient and sustainable alternative compared to widely used noble metals.[2−4] Copper(I) phosphide (Cu$_3$P), which is the focus of this work, is a p-type semiconductor with a bandgap of ∼1.50 eV.[5−7] The p-type semiconducting behavior of Cu$_3$P has its origin in the pronounced substoichiometry in Cu due to Cu vacancies, which has already been discussed in detail in previous studies.[8,9] A homogeneity range between approximately Cu$_{2.9}$P and Cu$_{2.3}$P has been reported,[10] making the use of the chemical formula Cu$_{3−x}$P more appropriate, and theoretical calculations suggest an increase of Cu vacancies with temperature.[8] Since we did not study the composition in detail, we will refer to Cu$_{3−x}$P as Cu$_3$P for simplicity. Cu-deficient Cu$_3$P shows a high performance as anode material for Li-ion batteries[10,11] and even exceeds the volumetric capacity of graphite.[12] Moreover, the self-doping of Cu$_3$P results in efficient and tunable light absorption in the near-infrared region due to localized surface plasmon resonance (LSPR).[5,8,9] The outstanding properties of

Cu$_3$P have enabled its application in various fields, including energy storage,[13−17] photodetection,[18] catalysis,[19] sensing,[20,21] ion exchange,[8,22] and cancer therapy.[23] Especially, the use of Cu$_3$P as a catalyst for the hydrogen evolution reaction (HER) is a promising and highly investigated research area.[24−33]

Recent studies reveal an increased photocatalytic activity when Cu$_3$P is combined with noble metals[34,35] or n-type semiconductors[6,7,33,36] due to efficient charge carrier separation by plasmon−exciton coupling[37,38] or an n-p heterojunction.[39,40] Various properties within the same nanocrystal, including the facet-dependent photocatalytic activity and the electronic band structure, point out the importance of a facet-engineered surface and heterointerface design.[41−43] The facet-dependent photocatalytic activity is well-described in the literature and caused by facet-varying reactant adsorption/product desorption as well as charge carrier separation/transfer characteristics.[44−48] Moreover, the surface termination of a crystal facet can vary with its

orientation and process conditions, which has an impact on the photocatalytic activity.[49] Additionally, the facets forming a heterointerface have been identified as an important factor for the performance of a metal−semiconductor heterostructure as a photocatalyst. This is due to the dependence of the surface work function on the crystal facet and the resulting ability to form the required Schottky junction.[50,51] The discussed potential of nanoparticle heterostructures is promoted by tremendous research efforts in this field.[52−54] To the best of our knowledge, the combination of Ag and Cu_3P with potential application in photocatalysis has not been investigated so far. Therefore, a detailed analysis of such nanoparticle heterostructures' structural and morphological evolution during the synthesis is required to tailor their properties and correlate them with their photocatalytic performance.

Our study aims to reveal the dynamic processes just before, during, and immediately after synthesizing Ag−Cu_3P nanoparticle heterostructures by *in situ* transmission electron microscopy (TEM). We performed the experiments by depositing Ag−Cu nanoparticle heterostructures on a heating chip, which we then transferred to an environmental transmission electron microscope (ETEM) with an integrated metal−organic chemical vapor deposition (MOCVD) system. The controlled supply of phosphine (PH_3) to Ag−Cu nanoparticle heterostructures with defined interfaces allowed for the observation of the Cu−Cu_3P phase transformation at moderate temperatures. We analyzed the dynamic processes involved in the phase transformation and characterized the present phases *via* high-resolution TEM (HRTEM) imaging, high frame rate TEM movies, and energy dispersive X-ray spectroscopy (EDS). The herein presented Ag−Cu_3P nanoparticle heterostructures have the potential to act, for instance, as high-performance photocatalysts for water splitting. Our results will help synthesize Ag−Cu_3P nanoparticle heterostructures with well-defined facets and heterointerfaces *via* a gas-phase process, enabling the evaluation of their impact on the optical properties/potential photocatalytic activity in future studies.

RESULTS AND DISCUSSION

For the formation of Ag−Cu_3P nanoparticle heterostructures, bimetallic Ag−Cu nanoparticles were generated in a spark ablation system,[55] and particles with a defined diameter of 30 nm were selected *via* an integrated filtering system for the deposition on a microelectromechanical systems (MEMS)-based heating chip for *in situ* TEM investigations. Subsequently, the chip was transferred to an ETEM with an integrated MOCVD system. The deposited bimetallic nanoparticles were heated to 350 °C and revealed phase separation with rough heterointerfaces and the presence of surface oxides/C-based contamination (see Figure S1). Therefore, the initially present oxides were reduced *via* a H_2 treatment at 500−650 °C, resulting in the complete removal of surface oxides and the formation of sharp heterointerfaces. The observation of a large number of Ag−Cu nanoparticle heterostructures with a sharp Ag{111}/Cu{111} interface (see Figure S2) is in good agreement with a previous experimental study performed under comparable conditions, in which the side-by-side orientation of the Ag and Cu phases connected *via* {111} facets was identified as the energetically most favorable structural configuration for the here applied size range.[56] However, for a minority of particles, twinned phases and rough heterointerfaces remained even after the H_2 annealing (see Figure S3).

Subsequently, the temperature was reduced to 350 °C, and PH_3 was supplied to the system to initiate the Cu−Cu_3P phase transformation. The analysis of heterointerfaces in the resulting Ag−Cu_3P nanoparticles suggests that the major product after the phase transformation had a Ag{111}/Cu_3P{3$\bar{3}$00} interface (see Figure S4). The preserved Ag{111} facet, in combination with the in-plane angular relation between the Ag and Cu phases as well as the Cu and Cu_3P phases (explained in detail below), suggests the initially present Ag{111}/Cu{111} interface acting as a template. Nevertheless, a minor fraction of nanoparticle heterostructures with different facets forming the Ag−Cu_3P interface has been observed, which indicates scenarios where the Ag{111}/Cu_3P{3$\bar{3}$00} interface cannot be maintained.

At this point, it was unclear if uncommon structural configurations of Ag−Cu_3P nanoparticle heterostructures are formed solely by Ag−Cu nanoparticles without a sharp Ag{111}/Cu{111} interface (see Figure S3) or if there is an alternative pathway for Ag−Cu nanoparticles with a sharp Ag{111}/Cu{111} interface. Therefore, a Ag−Cu nanoparticle heterostructure was tilted until the interface was oriented near-parallel to the electron beam and both phases oriented close to one of their zone axes (Figure 1). The power spectra shown as
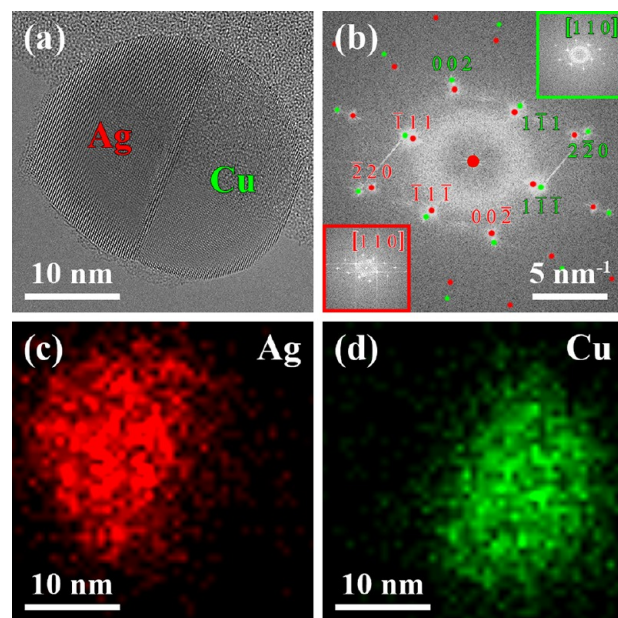

Figure 1. (a) HRTEM image of an Ag−Cu nanoparticle heterostructure acquired at 350 °C after H_2 treatment at 500 °C. (b) Corresponding power spectrum with overlaid simulated electron diffraction patterns[57] of the cubic Ag (red) and Cu (green) phases (space group: $Fm\bar{3}m$). The power spectra of Ag (red, bottom left) and Cu (green, top right) as insets in (b) highlight the successful tilting of both phases close to their [110] zone axes. Consequently, the heterointerface in (a) is near-parallel to the direction of the electron beam. (c) Ag ($L\alpha_1$) and (d) Cu ($K\alpha_1$) STEM-EDS elemental maps of the Ag−Cu nanoparticle heterostructure shown in (a).

insets in Figure 1b correspond to the cubic Ag (red) and Cu (green) phases and confirm the successful tilting close to their [110] zone axes. The acquired HRTEM image (Figure 1a) and the corresponding power spectrum with overlaid simulated electron diffraction patterns[57] of the Ag and Cu phases with space group $Fm\bar{3}m$ (Figure 1b) show their heterointerfacial connection *via* {111} facets. Note that the appearance of lattice fringes is not sensitive to small tilts up to a few degrees of the
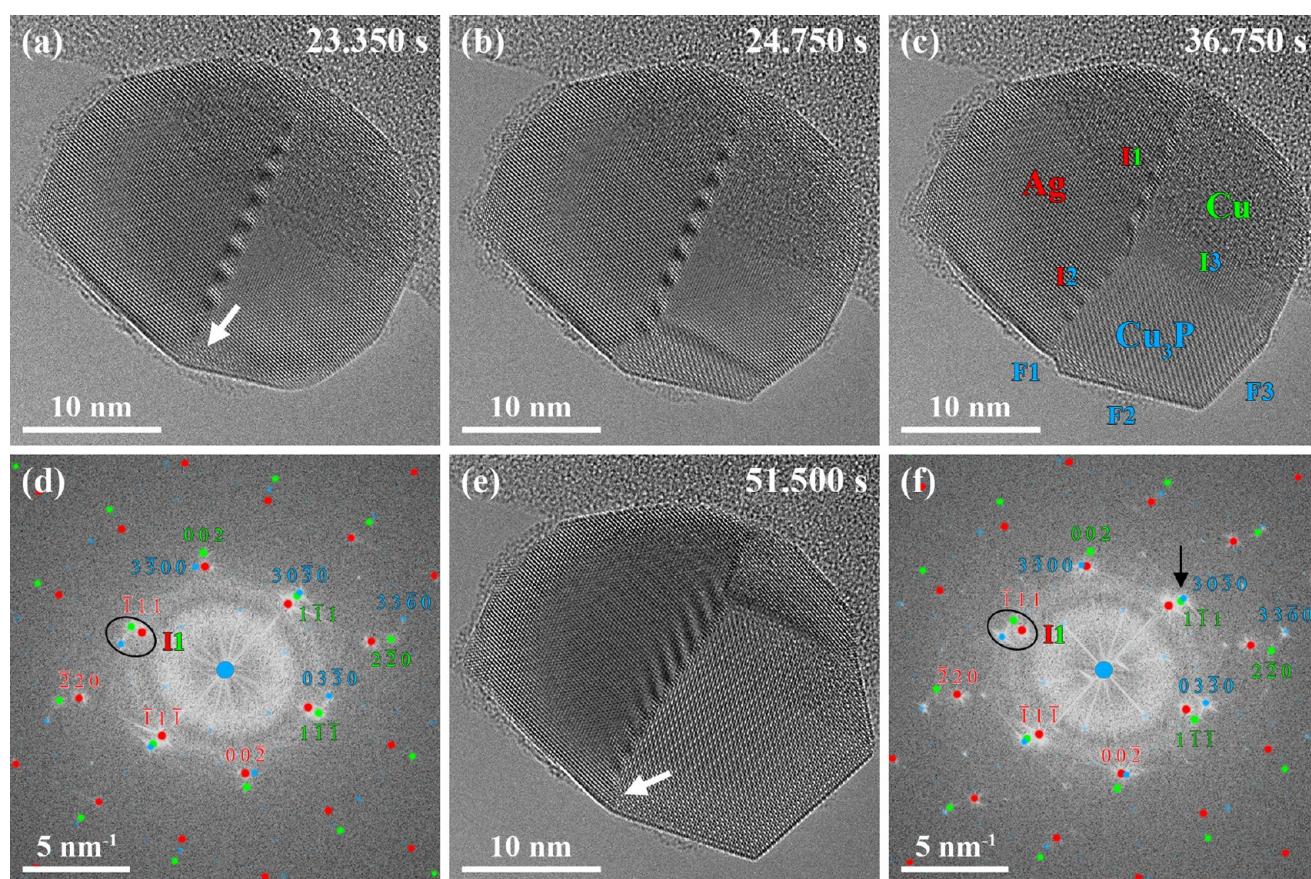
Figure 2. Selected averaged frames of a HRTEM movie (see Movie S1) at (a) 23.350 s, (b) 24.750 s, (c) 36.750 s, and (e) 51.500 s after the supply of PH_3 to the Ag−Cu nanoparticle heterostructure shown in Figure 1, which was kept at 350 °C. (a) Cu_3P phase nucleates at the triple-phase boundary indicated by a white arrow and (b) grows by consuming the Cu phase. (c) Phase transformation is far advanced, and the different phases, the heterointerfaces I1−3, and the Cu_3P facets F1−3 are highlighted. (d) Power spectrum corresponding to (c) with overlaid simulated electron diffraction patterns of the different phases[57,58] shows their crystallographic relation, and the black ellipse indicates the Ag($\bar{1}11$)/Cu($\bar{1}11$) heterointerface I1, which remains unaltered when compared to the power spectrum in Figure 1b. The Cu_3P phase (blue) is oriented close to its [0001] zone axis. (e) Strong fringes at the heterointerface I2 caused by strain effects are visible just before the complete transformation of the Cu phase. The white arrow highlights the wetting of the Cu_3P facet F1 by Ag as part of the structural rearrangement. (f) Simulated reflections in the black ellipse match with the power spectrum corresponding to (e) and show an anticlockwise in-plane rotation of the Ag phase relative to the Cu and Cu_3P phases when compared with those in (d). The Cu($\bar{1}11$) planes show an in-plane angular relation with Cu_3P($30\bar{3}0$) planes during the rearrangement, which is indicated by the black arrow in (f) and also observable in (d).

crystal away from the intended zone axes, given the imaging parameters and low thicknesses. Hence, we qualify their orientations as being close to [110]. However, note that, even with a few degrees of crystal tilt as observed for the nanoparticle heterostructure in Figure 1b, it is correct to say that the interface consists primarily of connected {111} planes, with the potential presence of a few steps to account for relative crystal tilts.[56] This analysis also applies to later examples of (near) parallel lattice planes at interfaces.

Moreover, scanning transmission electron microscopy (STEM)-EDS elemental maps acquired at 350 °C (Figure 1c,d) confirm the given attribution of the Ag and Cu phases. The selected area sum EDS spectra reveal the high purity of both phases noticeable by a low solubility of less than 3 atom % of Ag in Cu and *vice versa* (see Figure S5), which is in accordance with the Ag−Cu binary phase diagram.[59]

As part of the phase transformation experiment, an HRTEM movie (see Movie S1) of the same Ag−Cu nanoparticle heterostructure as highlighted in Figure 1 was acquired to capture the dynamic processes occurring straight after the supply of PH_3. A sequence of selected averaged frames of this

movie reveals a phase transformation of the Cu phase (Figure 2). The phase transformation started 23.350 s after the supply of PH_3 at the triple-phase boundary of the Ag−Cu nanoparticle heterostructure. A white arrow in Figure 2a indicates the location of the nucleation event of the new phase. The formed phase (Figure 2a−c) can be assigned to hexagonal Cu_3P (blue, space group: $P6_3cm$) oriented close to its [0001] zone axis *via* analysis of the power spectrum (Figure 2d) corresponding to the HRTEM image in Figure 2c. The formation of Cu_3P proceeded by consuming Cu at the Cu−Cu_3P interface (I3); however, a detailed analysis of the local atomic structure of this specific heterointerface is not possible due to the fast dynamic processes caused by the ongoing chemical reaction.

The Ag($\bar{1}11$)/Cu($\bar{1}11$) interface (I1) dominated the arrangement of the three phases in Figure 2c, which is indicated by the unaltered in-plane angular alignment of the corresponding Ag and Cu reflections in the black ellipse in Figure 2d when compared to Figure 1b. The formation of Cu_3P{$33\bar{6}0$} facets, which are highlighted as facets F1−3 in Figure 2c, are attributed to the Cu−Cu_3P phase transformation. This observation is consistent with previously reported faceting of Cu_3P nano-

particles with a similar size obtained by a solution-based approach including surface-active agents.[34] This leads to the conclusion that the different process conditions, including the presence of the Ag phase, the surrounding gas phase, and the low pressure in the ETEM, did not alter the facet evolution of the Cu_3P phase. It should be noted that facets F1−3 might also be formed by two different facets resulting in an edge, which is illustrated elsewhere.[60]

Moreover, the growth of the Cu_3P phase was accompanied by a volume expansion of ∼43% (related to the Cu phase) and caused a massive strain in the heterostructure (Figure 2e), resulting in fringes located in the Ag phase close to the Ag−Cu_3P interface (I2). Upon further progress of the phase transformation, the area of heterointerface I1 decreased (Figure 2e). A comparison of the corresponding reflections in the black ellipses in Figure 2d,f suggests the occurrence of an anticlockwise in-plane rotation of the Ag phase relative to the Cu and Cu_3P phases about the associated zone axis. It is worth mentioning that the $Cu(1\bar{1}1)$ planes showed an in-plane angular relation with the $Cu_3P(30\bar{3}0)$ planes during this rearrangement, indicated by the black arrow in Figure 2f and in agreement with a previous study on the Cu−Cu_3P phase transformation.[60] The increasing impact of the in-plane angular mismatch between the Ag and Cu_3P phases and the simultaneously decreasing area of heterointerface I1 might have been the driving force for the anticlockwise in-plane rotation of the Ag phase relative to the Cu and Cu_3P phases. Moreover, the relative in-plane rotation led to (or might have been initiated by) Ag wetting the facet F1, which is highlighted by a white arrow in Figure 2e.

A white arrow in Figure 3a indicates the remaining Cu phase 53.700 s after the supply of PH_3. The power spectrum obtained from the region highlighted by a white rectangle in Figure 3a and overlaid with simulated electron diffraction patterns from the involved phases reveals an alteration of the crystallographic arrangement of the phases in the last stage of the phase transformation (Figure 3b). The in-plane angular relation between the $Cu(1\bar{1}1)$ and $Cu_3P(30\bar{3}0)$ planes was slightly altered compared to Figure 2d,f. Instead, the phases were arranged so that the Ag, Cu, and Cu_3P reflections located within the black ellipses in Figure 3b have the same in-plane angular alignment. We believe that the alteration of the addressed in-plane angular relation between Cu and Cu_3P is the key step to form Ag−Cu_3P nanoparticle heterostructures with uncommon structural configurations discussed below.

In addition to the $Ag(\bar{1}11)/Cu_3P(0\bar{3}30)$ interface (I4), a new $Ag(\bar{2}20)/Cu_3P(\bar{3}3\bar{6}0)$ interface (I5) evolved after Cu had reacted completely with PH_3 to form Cu_3P (Figure 4a). Several incidents during the phase transformation, including the significant volume expansion during the Cu−Cu_3P phase transformation, the structural rearrangement of the phases just before the complete transformation (Figure 3), and the strained Ag phase at heterointerface I4, have been observed and might have contributed to the formation of heterointerface I5. However, we identified the presence of a defect in the Cu phase (see Figure S6) located in the region where heterointerface I5 started to grow, as the major difference to other Ag−Cu nanoparticle heterostructures and therefore as the potential origin of this observation. The assignment of heterointerfaces to the aforementioned planes does not strictly require that they are parallel. Minimal relative out-of-plane rotations cannot be ruled out on the basis of the appearance of the corresponding lattice fringes. However, these can be accommodated through steps or dislocations without changing the plane-types constituting the
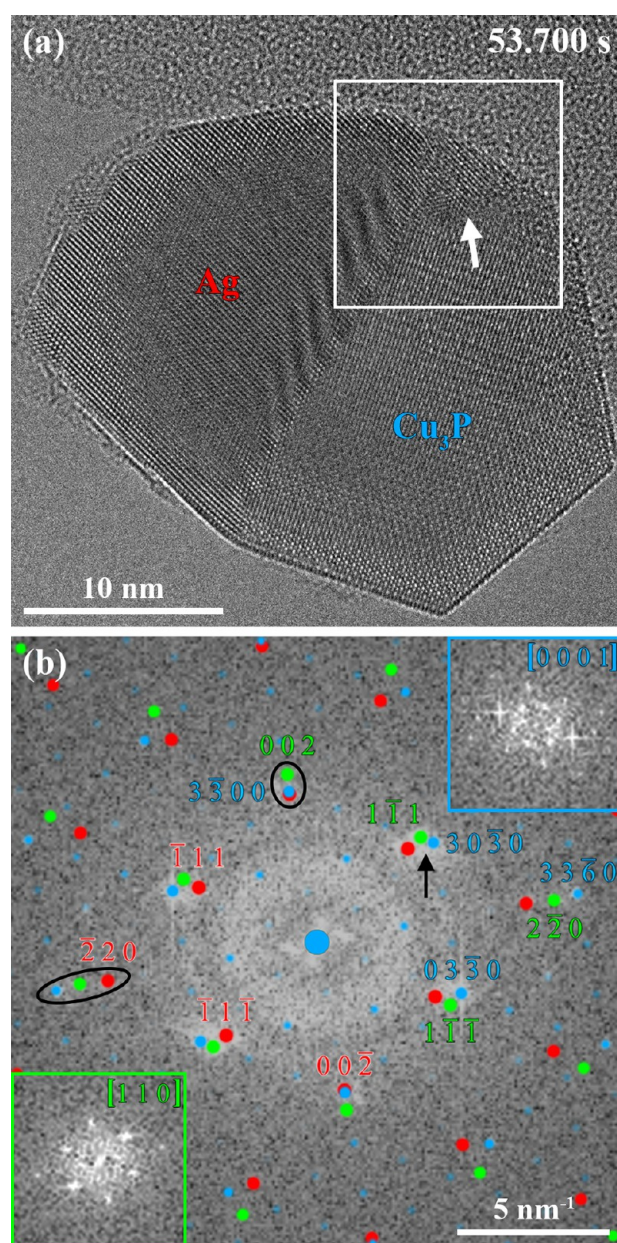

Figure 3. (a) Selected averaged frames of the same HRTEM movie used in Figure 2 (see Movie S1). The reaction between Cu and PH_3 is nearly completed 53.700 s after the supply of PH_3, and a white arrow indicates the location of the Cu phase. The power spectrum in (b) corresponds to the white rectangle in (a), and the overlaid simulated electron diffraction patterns of the three involved phases show that the in-plane angular relation between the $Cu(1\bar{1}1)$ and $Cu_3P(30\bar{3}0)$ planes is slightly altered (black arrow). Instead, the Ag, Cu, and Cu_3P reflections highlighted *via* black ellipses in (b) reveal a well-matching in-plane angular alignment. The power spectra of Cu (green, bottom left) and Cu_3P (blue, top right) are shown as insets in (b).

majority of the heterointerface. Analysis of the contrast in HRTEM images, detailed for the images acquired after the completion of the reaction, shows that any such out-of-plane rotations are minimal.

The appearance of heterointerface I5 prevented a free rotation of the phases, which is why fringes expanding over the Ag phase close to heterointerface I4 were still present after the consumption of Cu. In Ag−Cu_3P nanoparticle heterostructures with a single $Ag(\bar{1}11)/Cu_3P(0\bar{3}30)$ interface—and therefore
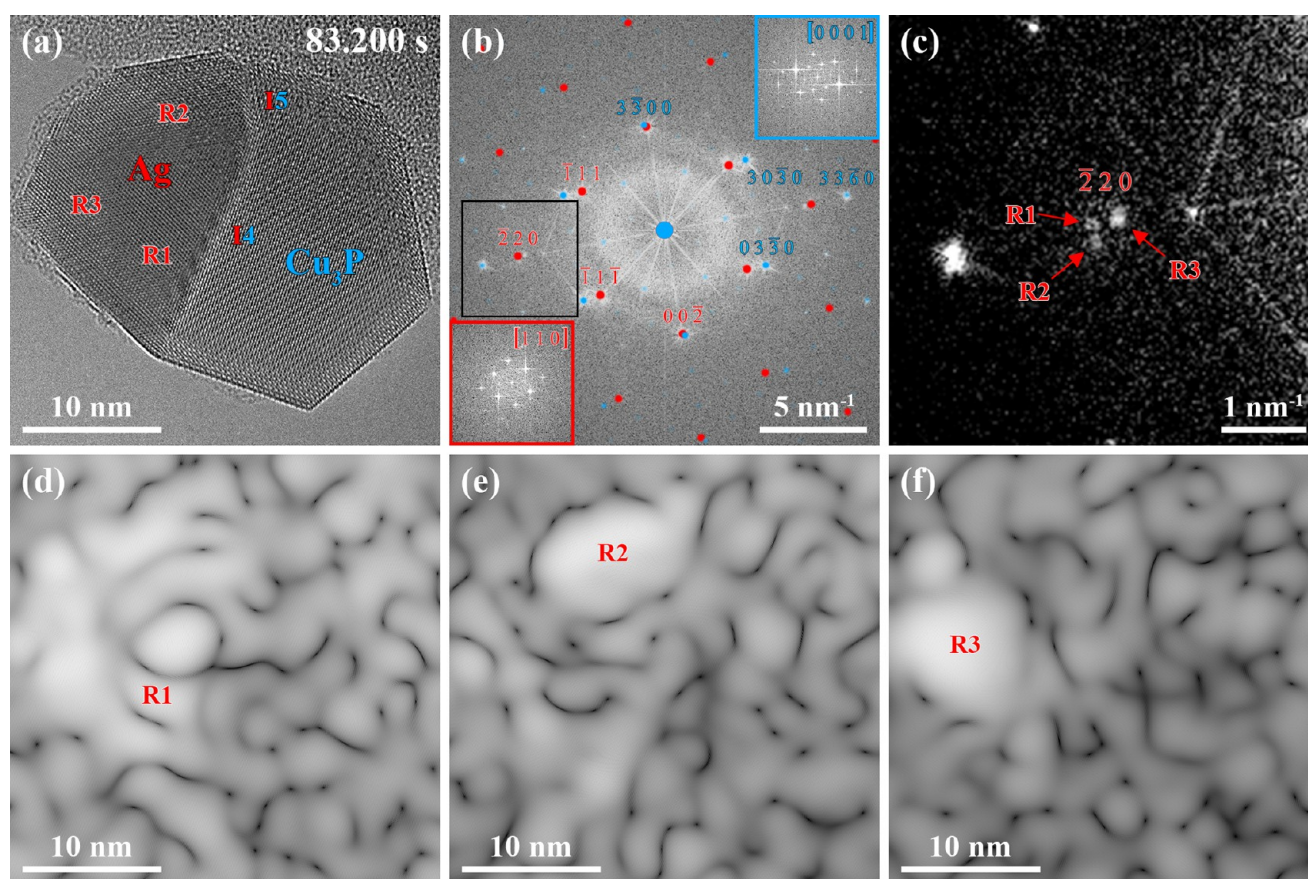
Figure 4. (a) Selected averaged frames of an HRTEM movie (see Movie S1) representing the state of the Ag–Cu$_3$P nanoparticle heterostructure 83.200 s after the supply of PH$_3$. The phase transformation is completed, and two heterointerfaces, I4 and I5, are visible. Moreover, fringes are located in the Ag phase close to heterointerface I4, which indicates strain effects. (b) Power spectrum corresponding to (a) with overlaid simulated Ag and Cu$_3$P electron diffraction patterns. The insets in (b) represent power spectra from the Ag (red, bottom left) and the Cu$_3$P (blue, top right) phases. (c) Zoomed-in section of the power spectrum (brightness and contrast adapted) indicated by a black rectangle in (b) shows the Ag($\bar{2}$20) reflections. Three slightly different Ag($\bar{2}$20) reflections labeled as regions R1–3 are highlighted by red arrows. (d–f) Inversed power spectra after applying a spot mask on (d) R1, (e) R2, and (f) R3 and their associated Ag($\bar{2}$20) reflections in the power spectrum in (b). The reflections in (c) can be assigned to different regions within the Ag phase, highlighted in (a).

the freedom of the phases to rotate—such fringes are not visible (see Figure S4). The power spectrum of the HRTEM image in Figure 4a confirms the complete consumption of the Cu phase, and the insets reveal that the Ag and the Cu$_3$P phases were still oriented close to their same zone axes (Figure 4b).

A closer look at the Ag($\bar{2}$20) reflections points out slight variations of corresponding planes in their in-plane orientation and/or interplanar spacing (Figure 4c). A spot mask on each of those three reflections has been applied, and subsequently, the obtained power spectra have been inversed (Figure 4d–f). Each set of reflections can be assigned to different regions R1–3 within the Ag phase. Region R1 is located close to the surface of the Ag phase and the area where Ag forms heterointerface I4. Region R2 can be associated with the Ag phase forming heterointerface I5, while region R3 is not in contact with the Cu$_3$P phase. Ag($\bar{2}$20) planes in regions R1 and R2 have similar interplanar spacings; however, an in-plane angular misfit exists. In contrast, Ag($\bar{2}$20) planes in regions R1 and R3 do not show an in-plane angular misfit, but the interplanar spacing is larger in region R3. The different regions in the Ag phase, also highlighted in Figure 4a, suggest an inhomogeneous strain distribution.

Subsequently, after the phase transformation, the nanoparticle heterostructure was kept at 350 °C for a longer period to investigate dynamic processes, including potential interface

rearrangement. The HRTEM image in Figure 5a shows the Ag–Cu$_3$P nanoparticle heterostructure 200 min after the PH$_3$ supply was started. The characterization *via* STEM-EDS confirms the exclusive chemical reaction of PH$_3$ with Cu under the chosen process conditions (see Figure S7), which is in good agreement with the ternary phase diagram.[61] Under the used conditions, the nanoparticle heterostructure underwent a structural rearrangement process, involving the growth of heterointerface I5 at the cost of heterointerface I4 (Figure 5a). Furthermore, corner truncation of the faceted Cu$_3$P phase has been observed over time, which is a well-described phenomenon reported for faceted nanoparticles upon thermal annealing and driven by the minimization of the total surface free energy.[62] We believe that this corner truncation is not related to the presence of multiple heterointerfaces since it was also observed for an Ag–Cu$_3$P nanoparticle heterostructure with a single heterointerface (see Figure S8).

A structural evaluation of the heterointerfaces I4 and I5 at an atomic level is possible *via* the reconstruction of the specimen exit wave function from a series of HRTEM images acquired at different defoci.[63] The phase image of the reconstructed exit wave function was used to prepare a strain map of the Ag–Cu$_3$P nanoparticle heterostructure. The spot masks for the geometrical phase analysis (GPA)[64] were centered at the Ag($1\bar{1}\bar{1}$)
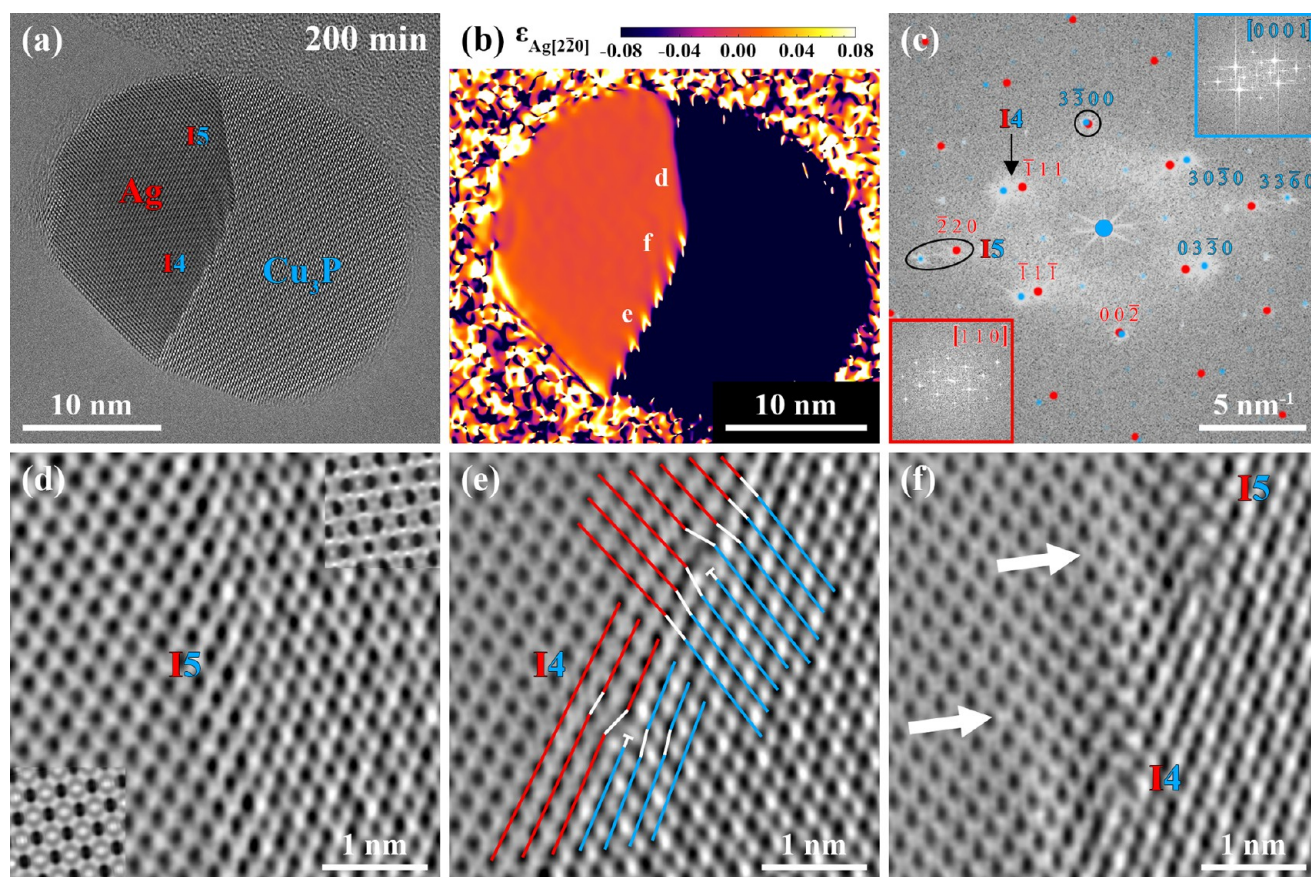
Figure 5. (a) HRTEM image of the same $Ag-Cu_3P$ nanoparticle heterostructure acquired 200 min after the start of the PH_3 supply. The temperature and the PH_3 flow remained unaltered during this period, and heterointerface I5 grew at the cost of heterointerface I4. (b) Strain map of the $Ag-Cu_3P$ nanoparticle heterostructure obtained from GPA of the phase image of the reconstructed exit wave function. The spot masks for the GPA were centered at the $Ag(1\overline{1}1)$ and $Ag(1\overline{1}\overline{1})$ reflections and the map visualizes strain in the $Ag[2\overline{2}0]/Cu_3P[3\overline{3}60]$ direction. The labels highlight the observed regions in (d−f). (c) Power spectrum corresponding to (a) with overlaid simulated electron diffraction patterns of the Ag and Cu_3P phases allows for the assignment of well-aligned $Ag(\overline{2}20)$ and $Cu_3P(\overline{3}360)$ planes forming heterointerface I5 (black ellipse). The matching Ag (red) and Cu_3P (blue) reflections in the black circle indicate that the planes perpendicular to heterointerface I5 have the same interplanar spacing in both phases, which could hint toward the origin of the rearrangement to a more stable configuration. The power spectra of the Ag (red, bottom left) and Cu_3P (blue, top right) phases are shown as insets of (c). (d) Phase image of heterointerface I5 with simulated phase images of the Ag (bottom left) and Cu_3P (top right) phases as insets. (e) Phase image of the stepped heterointerface I4. Red (Ag) and blue (Cu_3P) lines indicate the presence of dislocations due to lattice misfit. $Ag(1\overline{1}1)$ and $Cu_3P(0\overline{3}30)$ planes straight at the heterointerface have a parallel in-plane alignment while showing an in-plane rotation further away from the heterointerface. (f) Phase image with fringes (indicated by white arrows) due to strain effects evolving in the Ag phase parallel to heterointerface I5.

and $Ag(1\overline{1}1)$ reflections. Due to the close proximity of the $Cu_3P(0\overline{3}30)$ and $Cu_3P(30\overline{3}0)$ reflections, the Cu_3P phase was also included in the strain map. The strain across the nanoparticle heterostructure in the $Ag[2\overline{2}0]$ and corresponding $Cu_3P[3\overline{3}\overline{6}0]$ direction is visualized in Figure 5b and shows the different interplanar spacings of the different phases.

The strain map highlights the current conditions at and around the heterointerfaces. For heterointerface I5, a sharp transition from one phase to the other is observed. The well-matching Ag and Cu_3P reflections in the black ellipse in the power spectrum corresponding to Figure 5a (Figure 5c) suggest that parallel $Ag(\overline{2}20)$ and $Cu_3P(\overline{3}360)$ planes form heterointerface I5 (Figure 5d). A minimal out-of-plane rotation of the two phases relative to each other cannot be ruled out based solely on the appearance of the described reflections. However, through comparisons of experimental data and simulations (HRTEM and selected area electron diffraction (SAED)), crystal tilts of both phases off the specific zone axes are determined to have the same direction and the same magnitude of less than 1.6° (see

Figures S9−S14). The combination of those results (axis of the rotation is normal to heterointerface I5) and the lack of Moiré fringes observed at heterointerface I5 allows for the exclusion of any out-of-plane rotations. Additionally, heterointerface I5 completely lacks the strain fields observed at heterointerface I4 due to its low-angle mismatch (see below). This supports the assignment of a parallel $Ag(\overline{2}20)/Cu_3P(\overline{3}360)$ interface for heterointerface I5.

Moreover, the $Ag(002)$ and $Cu_3P(\overline{3}300)$ reflections overlap, highlighted by the black circle in Figure 5c. Consequently, the associated planes $(Ag(002)$ and $Cu_3P(\overline{3}300))$ perpendicular to heterointerface I5 have the same interplanar spacings. This may explain why heterointerface I5 is energetically more favorable than heterointerface I4, which is a kinetic product and formed due to the initially present $Ag(\overline{1}11)/Cu(\overline{1}11)$ interface acting as a template.

In contrast, the combination of a strain map (Figure 5b) and HRTEM image (Figure 5a) reveals a stepped heterointerface I4 with fringes evolving into the Ag phase. The black arrow in the

power spectrum corresponding to Figure 5a highlights the in-plane angular misfit of the Ag($\bar{1}$11) and Cu$_3$P(0$\bar{3}$30) planes being involved in the formation of heterointerface I4 (Figure 5c). The phase image in Figure 5e reveals a series of misfit dislocations, highlighted by white symbols (T) in Figure 5e, causing the stepped appearance of heterointerface I4. In the here presented case, the dislocations are arranged so that, at each indicated position, both types of differently oriented dislocation lines share the same core (only one type per position indicated).

The complex arrangement of misfit dislocations allows for the accommodation of strain caused by lattice mismatch. Accommodation of strain *via* the formation of dislocations is a well-known mechanism in nanoscale heterostructures.[65,66] More-over, the addressed arrangement of line defects enables a more parallel alignment of planes straight at heterointerface I4 to overcome the in-plane angular misalignment of Ag($\bar{1}$11) and Cu$_3$P(0$\bar{3}$30) planes further away from the heterointerface. This is indicated by the red (Ag) and blue (Cu$_3$P) lines in Figure 5e. Additionally, the defective heterointerface I4 leads to strain in the Ag phase along the Ag[2$\bar{2}$0] direction, which is indicated by white arrows in the phase image in Figure 5f. Besides the in-plane angular misalignment of planes forming heterointerface I4, a comparison of heterointerface I4 (Figure 5) with other nanoparticle heterostructures exhibiting just a single hetero-interface formed by the same Ag and Cu$_3$P planes (see Figure S4) hints toward a slight rotation of heterointerface I4's phases against each other, away from the favorable configuration (see Figure S15).

The incoherent heterointerface I4 enabled the efficient diffusion of atoms toward heterointerface I5 due to its high mobility. However, the structural rearrangement of the phases at 350 °C was not finished 217 min after starting the PH$_3$ supply. Therefore, the temperature was increased to 500 °C with a heating rate of 5 °C/s to accelerate the rearrangement, and the dynamic processes were tracked by acquiring a HRTEM movie. Heterointerface I5 has almost completely replaced heterointer-face I4 during the heating (see Movie S2). After reaching 500 °C, the Ag−Cu$_3$P nanoparticle heterostructure reached its stable configuration and heterointerface I4 disappeared, as shown in the HRTEM image in Figure 6a. The final structure did not show fringes expanding from the heterointerface, which hints toward a fully coherent heterointerface. The corresponding power spectrum in Figure 6b only shows minor alterations (the orientation of the nanoparticle heterostructure changed slightly) when compared to the power spectrum of the Ag−Cu$_3$P nanoparticle heterostructure before the heat treatment at 500 °C (Figure 5c).

It is also worth mentioning that the presence of C-based contamination (mainly on the Ag surface) was observed during the experiment. This is a well-known observation in electron microscopy and caused by the electron beam in combination with the presence of organic molecules.[67] Surface contamination could have an impact on the evolution of the Ag facets and, therefore, could contribute to structural rearrangement processes. Furthermore, the energy input by electrons from the electron beam could accelerate the dynamic processes reported in this study. Nevertheless, our study points out the potential of facet-engineered surface and heterointerface design in Ag−Cu$_3$P nanoparticle heterostructures by controlling the structural evolution of Ag−Cu nanoparticle templates (e.g., by adapting the particle size[56]) and/or thermal annealing.
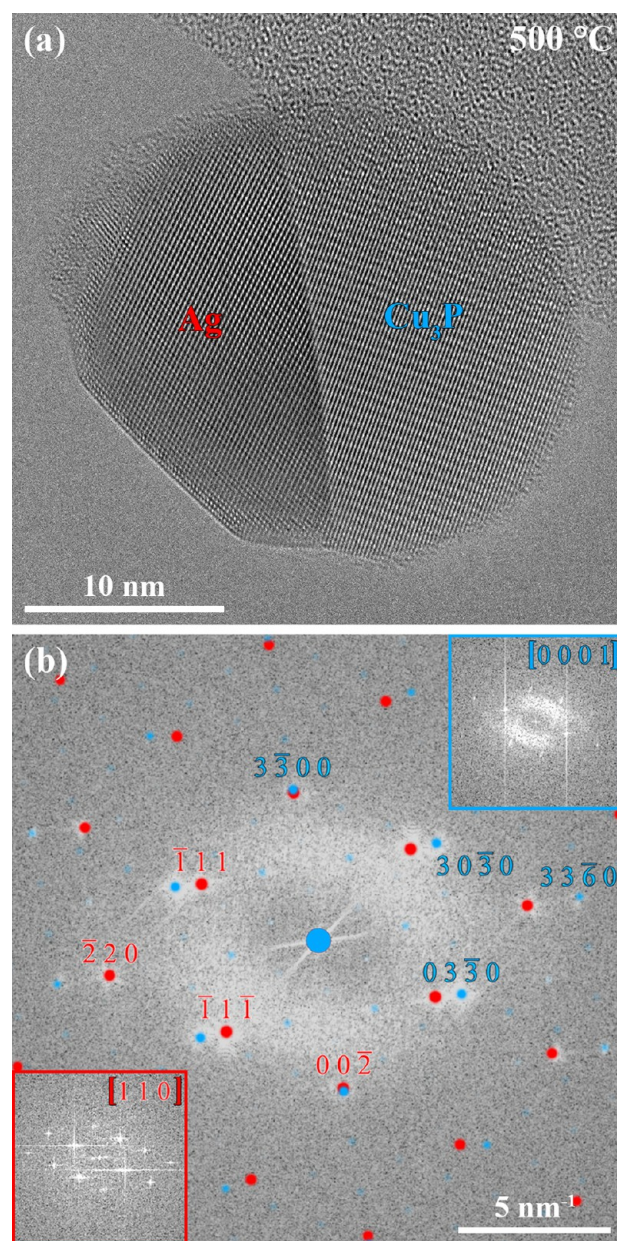

Figure 6. (a) HRTEM image of the same Ag−Cu$_3$P nanoparticle heterostructure after increasing the temperature to 500 °C shows the complete replacement of heterointerface I4 by heterointerface I5. (b) Power spectrum corresponding to (a) with overlaid simulated electron diffraction patterns of the Ag and Cu$_3$P phases. The thermal expansion of the Ag phase upon heating the sample to 500 °C has been considered for the simulation. The insets in (b) reveal selected area power spectra of the Ag (red, bottom left) and Cu$_3$P (blue, top right) phases.

■ CONCLUSIONS

Our results enlighten the dynamic processes that occurred in Ag−Cu nanoparticle heterostructures with a Ag{111}/Cu{111} interface during PH$_3$ exposure at 350 °C. The Ag phase did not react with PH$_3$ under the used process conditions, while the Cu phase showed a phase transformation into Cu$_3$P. Ag−Cu$_3$P nanoparticle heterostructures with a single Ag{111}/Cu$_3$P-{3$\bar{3}$00} interface were the most common product of this synthesis procedure due to Ag−Cu nanoparticle heterostruc-tures with Ag{111} and Cu{111} facets forming a defined interface acting as a template.

However, in a specific case, we observed dynamic processes leading to the structural rearrangement of the nanoparticle heterostructure. At the beginning of the phase transformation, the arrangement of the three-phase nanoparticle was dominated by the Ag($\bar{1}$11)/Cu($\bar{1}$11) interface. At a later stage of the transformation, when the Ag/Cu interface area decreased, we observed an in-plane rotation of the Ag phase relative to the Cu and Cu$_3$P phases that reduced the in-plane angular misfit between the Ag and Cu$_3$P phases. Further, the Cu(1$\bar{1}$1) and Cu$_3$P(30$\bar{3}$0) planes showed an in-plane angular relation during the transformation. In the last steps of the Cu−Cu$_3$P phase transformation, when the Cu phase was almost completely consumed, the in-plane angular relation between the Cu(1$\bar{1}$1) and Cu$_3$P(30$\bar{3}$0) planes was slightly altered and an additional heterointerface—formed by Ag($\bar{2}$20) and Cu$_3$P($\bar{3}3\bar{6}0$) planes—appeared. We believe that the formation of the Ag($\bar{2}$20)/Cu$_3$P($\bar{3}3\bar{6}0$) interface was caused by an initially present defect in the Cu phase.

Once the Ag($\bar{2}$20)/Cu$_3$P($\bar{3}3\bar{6}0$) interface had formed, a structural rearrangement of the phases occurred, which led to the stepwise disappearance of the Ag($\bar{1}$11)/Cu$_3$P(0$\bar{3}$30) interface. Our findings show that a potential reason the Ag($\bar{2}$20)/Cu$_3$P($\bar{3}3\bar{6}0$) interface was energetically favored during the rearrangement process can be found in the matching interplanar spacing for planes perpendicular to the addressed heterointerface. Moreover, the simultaneous presence of both heterointerfaces within the same Ag−Cu$_3$P nanoparticle led to an inhomogeneous strain distribution within the Ag phase, which might have destabilized the nanoparticle heterostructure and driven the rearrangement process. Furthermore, we observed corner truncation of the faceted Cu$_3$P phase over time to reduce the total surface free energy.

We increased the temperature to 500 °C to accelerate the slow rearrangement of the Ag−Cu$_3$P nanoparticle at 350 °C and obtained a single Ag($\bar{2}$20)/Cu$_3$P($\bar{3}3\bar{6}0$) interface within the heterostructure after the temperature treatment. The absence of strain fields suggests the presence of a fully coherent heterointerface. The presented results on interface dynamics in Ag−Cu$_3$P nanoparticle heterostructures highlight the potential to select specific interfaces in metal−semiconductor heterostructures using templates and varying process parameters. This will help evaluate the impact of their tailored structural and morphological properties on their photocatalytic performance in future experiments.

■ METHODS

Ag−Cu Nanoparticle Synthesis and Deposition on MEMS-Based Heating Chips. A home-built spark ablation system with Ag as an anode and Cu as a cathode was used to form bimetallic agglomerates. A N$_2$/H$_2$ gas flow carried the bimetallic agglomerates from the spark through a furnace for sintering at 850 °C. A differential mobility analyzer system enabled the selection of sintered bimetallic nanoparticles with a diameter of 30 nm for the electrostatic deposition on MEMS-based heating chips. The parameters used for the synthesis and deposition of Ag−Cu nanoparticle heterostructures are in accordance with the parameters used in a recently published study.[55]

MEMS-Based Heating Chips for *in Situ* TEM Investigations. MEMS-based heating chips supplied by Norcada were used for *in situ* TEM investigations. The chips consist of a thin SiN$_x$ membrane with an embedded W heating coil for Joule heating. The temperature profile is homogeneous in the central region of the chip, and temperatures up to 1100 °C are achievable. The central region of the chip consists of 19 holes in the SiN$_x$ membrane with a thin SiN$_x$ region next to those holes. The Blaze software supplied by Hitachi enables the controlled variation

of the temperature in the central region of the chip *via* a constant resistance mode.

ETEM, TEM Imaging/Movies, and Characterization. The study was performed in a Hitachi HF-3300S ETEM operated at 300 kV. The microscope is equipped with a cold field emission gun and an imaging aberration corrector (CEOS BCOR). A scanning unit enables STEM imaging (annular dark field, bright field, and a secondary electron detector) as well as compositional microanalysis with EDS. The integrated complementary metal−oxide−semiconductor (CMOS) camera (GATAN OneView IS camera) allows for the investigation of dynamic processes by recording HRTEM movies with up to 300 frames/s. An electron dose rate in the range 1000−10 400 e/Å^2 s was used to acquire TEM images and movies (see Tables S1 and S2). Acquisition parameters used for STEM-EDS elemental maps and high-angle annular dark field (HAADF)-STEM images can be found in Tables S3 and S4. The background pressure next to the sample was ~1.6·10^{-4} Pa. Furthermore, the nanoparticle heterostructure presented in Figures 1−6 was exposed to a maximum electron dose of ~1.15·10^8 e/Å^2 throughout the whole experiment. Additional information about the ETEM in Lund is available elsewhere.[68]

Sample Holder and Precursor Supply. Experiments focused on the formation of Ag−Cu$_3$P nanoparticles were performed on a custom-built double tilt holder from Hitachi. Mass flow controllers integrated into the gas handling system enabled the controlled supply of PH$_3$ directly to the heated area of the MEMS-based heating chip inside the ETEM *via* a side port injector integrated into the microscope column.

Formation of Ag−Cu$_3$P Nanoparticles. The as-deposited Ag−Cu nanoparticles were heated to 500−650 °C, and 2.0 sccm H$_2$ (8.9·10^{-2} mmol/min, estimated pressure next to sample: ~1 Pa) was supplied for ~5 min *via* the side port injector. The gun valve remained closed during the H$_2$ treatment. Subsequently, the temperature was reduced to 350 °C. The H$_2$ treatment yielded a high amount of Ag−Cu nanoparticle heterostructures with a single interface and free from surface contamination. In the next step, 0.2 sccm PH$_3$ (9·10^{-3} mmol/min, estimated pressure next to sample: ~6.5·10^{-2} Pa) was supplied to initiate the phase transformation of Cu to Cu$_3$P. Finally, the temperature was increased to 500 °C with a heating rate of 5 °C/s to accelerate the growth of the favored heterointerface I5 at the cost of heterointerface I4.

Multislice Simulations and Exit Wave Function Reconstructions. A stack of 21 HRTEM images in the defocus range from −10 to 10 nm with a defocus step of 1 nm for both the Ag[110][57] and Cu$_3$P[0001][58] projections were simulated. Parameters used for the multislice simulations can be found in Table S5. The images of the simulated image stacks and the acquired focus series (see Table S6) were aligned. Subsequently, for each aligned image stack, an iterative wave function reconstruction was performed. The obtained exit wave functions were used to refine the alignment of the corresponding image stack. In total, three refinement−reconstruction cycles were performed for each image stack. The obtained exit wave functions were slightly adjusted *via* the integrated aberration corrector. Parameters used for the exit wave function reconstructions can be found in Table S7.

Geometrical Phase Analysis. The phase image of the reconstructed exit wave function was used to perform a GPA. The Cu$_3$P($\bar{1}1\bar{2}0$) reflection was selected as the smallest g-vector in the power spectrum. The Ag(11$\bar{1}$) and Ag(1$\bar{1}$1) reflections were chosen as g-vectors to prepare the strain map. Refinement was performed in the central region of the Ag phase. The axes were rotated in such a way that the x-axis is equal to the Ag[$\bar{2}$20] direction (vector addition of both chosen g-vectors). The strain map visualizes strain in the Ag[$\bar{2}$20] direction, and the strain limits were set to ±0.08.

Simulation of Electron Diffraction Patterns. For each power spectrum, the associated scale bar was used to determine the camera length for the simulation of the electron diffraction pattern. Further parameters used for the simulation of electron diffraction patterns can be found in Table S8. The expansion of the lattice at different temperatures has been considered for the electron diffraction pattern simulations of cubic Ag and Cu by using thermal expansion coefficients found in the literature.[57] In contrast to the Ag and Cu phases, the thermal expansion of Cu$_3$P upon heating was not considered for the

simulation of the associated electron diffraction pattern due to the missing thermal expansion coefficient of hexagonal Cu_3P in the literature.

Data Processing/Software. TEM images and movies (In-situ player) were acquired and processed with DigitalMicrograph from Gatan (Version 3.43.3213.0). For the HRTEM images extracted from Movie S1, the specific frames associated with selected times were averaged with the same amount of frames straight before and after the event (making a total of 11 (Figures 2 and 4)/3 (Figure 3) consecutive frames for averaging). Power spectra obtained from DigitalMicrograph were overlaid with simulated electron diffraction patterns using SingleCrystal from CrystalMaker Software Ltd. (Version 4.1.0). Atomic models were built with CrystalMaker from CrystalMaker Software Ltd. (Version 4.1.0). For acquiring and processing HAADF-STEM and EDS data, AZtec from Oxford Instruments Nanotechnology Tools Ltd. (Version 3.3) was used. Multislice simulations were performed with jems from P. Stadelmann (Version 4.9131U2020b31). Strain++ (Version 1.6), maintained by J. J. P. Peters, was used to prepare strain maps. In this software, strain is measured using a GPA algorithm described in the literature.[64] The exit wave function reconstructions were performed with IWFR for DigitalMicrograph from HREM Research Inc. (Version 2.0). Figures for this publication were prepared using Adobe Photoshop from Adobe (Version 22.1.0). Movies in the Supporting Information were compressed using ImageJ (Version 1.52a).

■ ASSOCIATED CONTENT

Ⓢ Supporting Information

The Supporting Information is available free of charge at https://pubs.acs.org/doi/10.1021/jacs.1c09179.

> Figures of HRTEM images, STEM-EDS elemental maps, power spectra, EDS sum spectra, HAADF-STEM image, HRTEM simulations for the Cu_3P phase, comparison of experimental data with simulations for the Cu_3P phase, HRTEM simulations for the Ag phase, comparison of experimental data with simulations for the Ag phase, confirmation of the comparisons' validity using the squared moduli of the Fourier transform of the exit wave function and simulated SAED patterns for the estimated tilts around specific crystal directions, and atomic models of the $Ag(\bar{1}11)/Cu_3P(0\bar{3}30)$ interface and tables of (acquisition) parameters used for HRTEM images and movies, STEM-EDS elemental maps, HAADF-STEM images, multislice simulations, the acquired focus series, exit wave function reconstructions, and simulations of electron diffraction patterns (PDF)

> Movie of $Cu–Cu_3P$ phase transformation corresponding to Figures 2–4 (AVI)

> Movie of replacement of heterointerface I4 by heterointerface I5 during temperature increase to 500 °C (AVI)

■ AUTHOR INFORMATION

Corresponding Authors

Michael S. Seifner − *Centre for Analysis and Synthesis and NanoLund, Lund University, 22100 Lund, Sweden;* ⓞ orcid.org/0000-0001-9101-5520; Email: Michael.Seifner@chem.lu.se

Kimberly A. Dick − *Centre for Analysis and Synthesis and NanoLund, Lund University, 22100 Lund, Sweden;* ⓞ orcid.org/0000-0003-4125-2039; Email: Kimberly.Dick_Thelander@chem.lu.se

Authors

Markus Snellman − *NanoLund and Solid State Physics, Lund University, 22100 Lund, Sweden;* ⓞ orcid.org/0000-0001-9519-9478

Ofentse A. Makgae − *Centre for Analysis and Synthesis and NanoLund, Lund University, 22100 Lund, Sweden;* ⓞ orcid.org/0000-0002-1664-9416

Krishna Kumar − *Centre for Analysis and Synthesis and NanoLund, Lund University, 22100 Lund, Sweden;* ⓞ orcid.org/0000-0001-8490-7897

Daniel Jacobsson − *Centre for Analysis and Synthesis, NanoLund, and National Center for High Resolution Electron Microscopy, Lund University, 22100 Lund, Sweden;* ⓞ orcid.org/0000-0001-5774-5116

Martin Ek − *Centre for Analysis and Synthesis and NanoLund, Lund University, 22100 Lund, Sweden;* ⓞ orcid.org/0000-0002-5705-8495

Knut Deppert − *NanoLund and Solid State Physics, Lund University, 22100 Lund, Sweden;* ⓞ orcid.org/0000-0002-0471-951X

Maria E. Messing − *NanoLund and Solid State Physics, Lund University, 22100 Lund, Sweden;* ⓞ orcid.org/0000-0003-1834-236X

Complete contact information is available at:
https://pubs.acs.org/10.1021/jacs.1c09179

Notes
The authors declare no competing financial interest.

■ ACKNOWLEDGMENTS

■ ABBREVIATIONS USED

TMP; transition metal phosphide; LSPR; localized surface plasmon resonance; HER; hydrogen evolution reaction; TEM; transmission electron microscopy; ETEM; environmental transmission electron microscope; MOCVD; metal−organic chemical vapor deposition; HRTEM; high-resolution transmission electron microscopy; EDS; energy dispersive X-ray spectroscopy; MEMS; microelectromechanical systems; STEM; scanning transmission electron microscopy; GPA; geometrical phase analysis; SAED; selected area electron diffraction; CMOS; complementary metal−oxide−semiconductor; HAADF; high-angle annular dark field

■ REFERENCES

(1) Shi, Y.; Li, M.; Yu, Y.; Zhang, B. Recent advances in nanostructured transition metal phosphides: synthesis and energy-related applications. *Energy Environ. Sci.* **2020**, *13* (12), 4564−4582.

(2) Callejas, J. F.; Read, C. G.; Roske, C. W.; Lewis, N. S.; Schaak, R. E. Synthesis, Characterization, and Properties of Metal Phosphide Catalysts for the Hydrogen-Evolution Reaction. *Chem. Mater.* **2016**, *28* (17), 6017−6044.

(3) Li, Y.; Dong, Z.; Jiao, L. Multifunctional Transition Metal-Based Phosphides in Energy-Related Electrocatalysis. *Adv. Energy Mater.* **2020**, *10* (11), 1902104.

(4) Pei, Y.; Cheng, Y.; Chen, J.; Smith, W.; Dong, P.; Ajayan, P. M.; Ye, M.; Shen, J. Recent developments of transition metal phosphides as catalysts in the energy conversion field. *J. Mater. Chem. A* **2018**, *6* (46), 23220−23243.

(5) Manna, G.; Bose, R.; Pradhan, N. Semiconducting and plasmonic copper phosphide platelets. *Angew. Chem., Int. Ed.* **2013**, *52* (26), 6762−6766.

(6) Yue, X.; Yi, S.; Wang, R.; Zhang, Z.; Qiu, S. A novel and highly efficient earth-abundant Cu_3P with TiO_2 "P-N" heterojunction nanophotocatalyst for hydrogen evolution from water. *Nanoscale* **2016**, *8* (40), 17516−17523.

(7) Qin, Z.; Wang, M.; Li, R.; Chen, Y. Novel $Cu_3P/g-C_3N_4$ p-n heterojunction photocatalysts for solar hydrogen generation. *Sci. China Mater.* **2018**, *61* (6), 861−868.

(8) De Trizio, L.; Gaspari, R.; Bertoni, G.; Kriegel, I.; Moretti, L.; Scotognella, F.; Maserati, L.; Zhang, Y.; Messina, G. C.; Prato, M.; Marras, S.; Cavalli, A.; Manna, L. $Cu_{3−x}P$ Nanocrystals as a Material Platform for Near-Infrared Plasmonics and Cation Exchange Reactions. *Chem. Mater.* **2015**, *27* (3), 1120−1128.

(9) Bertoni, G.; Ramasse, Q.; Brescia, R.; De Trizio, L.; De Donato, F.; Manna, L. Direct Quantification of Cu Vacancies and Spatial Localization of Surface Plasmon Resonances in Copper Phosphide Nanocrystals. *ACS Mater. Lett.* **2019**, *1* (6), 665−670.

(10) Wolff, A.; Doert, T.; Hunger, J.; Kaiser, M.; Pallmann, J.; Reinhold, R.; Yogendra, S.; Giebeler, L.; Sichelschmidt, J.; Schnelle, W.; Whiteside, R.; Gunaratne, H. Q. N.; Nockemann, P.; Weigand, J. J.; Brunner, E.; Ruck, M. Low-Temperature Tailoring of Copper-Deficient $Cu_{3−x}P$—Electric Properties, Phase Transitions, and Performance in Lithium-Ion Batteries. *Chem. Mater.* **2018**, *30* (20), 7111−7123.

(11) Stan, M. C.; Klöpsch, R.; Bhaskar, A.; Li, J.; Passerini, S.; Winter, M. Cu_3P Binary Phosphide: Synthesis via a Wet Mechanochemical Method and Electrochemical Behavior as Negative Electrode Material for Lithium-Ion Batteries. *Adv. Energy Mater.* **2013**, *3* (2), 231−238.

(12) Pfeiffer, H.; Tancret, F.; Bichat, M.-P.; Monconduit, L.; Favier, F.; Brousse, T. Air stable copper phosphide (Cu_3P): a possible negative electrode material for lithium batteries. *Electrochem. Commun.* **2004**, *6* (3), 263−267.

(13) Fan, M.; Chen, Y.; Xie, Y.; Yang, T.; Shen, X.; Xu, N.; Yu, H.; Yan, C. Half-Cell and Full-Cell Applications of Highly Stable and Binder-Free Sodium Ion Batteries Based on Cu_3P Nanowire Anodes. *Adv. Funct. Mater.* **2016**, *26* (28), 5019−5027.

(14) Chen, Y.-C.; Chen, Z.-B.; Lin, Y.-G.; Hsu, Y.-K. Synthesis of Copper Phosphide Nanotube Arrays as Electrodes for Asymmetric Supercapacitors. *ACS Sustainable Chem. Eng.* **2017**, *5* (5), 3863−3870.

(15) Jin, Y.; Zhao, C.; Wang, Y.; Jiang, Q.; Ji, C.; Jia, M. Large-scale production of Cu_3P nanocrystals for ultrahigh-rate supercapacitor. *Ionics* **2017**, *23* (11), 3249−3254.

(16) Li, G.; Tu, J.; Wang, M.; Jiao, S. Cu_3P as a novel cathode material for rechargeable aluminum-ion batteries. *J. Mater. Chem. A* **2019**, *7* (14), 8368−8375.

(17) Kumar, S.; Aziz, S. K. T.; Kumar, S.; Riyajuddin, S.; Yaniv, G.; Meshi, L.; Nessim, G. D.; Ghosh, K. Three-Dimensional Graphene-Decorated Copper-Phosphide ($Cu_3P@3DG$) Heterostructure as an Effective Electrode for a Supercapacitor. *Front. Mater.* **2020**, *7*, 30.

(18) Sun, T.; Wang, Y.; Yu, W.; Wang, Y.; Dai, Z.; Liu, Z.; Shivananju, B. N.; Zhang, Y.; Fu, K.; Shabbir, B.; Ma, W.; Li, S.; Bao, Q. Flexible Broadband Graphene Photodetectors Enhanced by Plasmonic $Cu_{3−x}P$ Colloidal Nanocrystals. *Small* **2017**, *13* (42), 1701881.

(19) Downes, C. A.; Libretto, N. J.; Harman-Ware, A. E.; Happs, R. M.; Ruddy, D. A.; Baddour, F. G.; Ferrell, J. R., III; Habas, S. E.; Schaidle, J. A. Electrocatalytic CO_2 Reduction over Cu_3P Nanoparticles Generated via a Molecular Precursor Route. *ACS Appl. Energy Mater.* **2020**, *3* (11), 10435−10446.

(20) Li, Z.; Xin, Y.; Wu, W.; Fu, B.; Zhang, Z. Topotactic Conversion of Copper(I) Phosphide Nanowires for Sensitive Electrochemical Detection of H_2O_2 Release from Living Cells. *Anal. Chem.* **2016**, *88* (15), 7724−7729.

(21) Xie, L.; Asiri, A. M.; Sun, X. Monolithically integrated copper phosphide nanowire: An efficient electrocatalyst for sensitive and

(22) Koh, S.; Kim, W. D.; Bae, W. K.; Lee, Y. K.; Lee, D. C. Controlling Ion-Exchange Balance and Morphology in Cation Exchange from $Cu_{3−x}P$ Nanoplatelets into InP Crystals. *Chem. Mater.* **2019**, *31* (6), 1990−2001.

(23) Liu, Y.; Wu, J.; Jin, Y.; Zhen, W.; Wang, Y.; Liu, J.; Jin, L.; Zhang, S.; Zhao, Y.; Song, S.; Yang, Y.; Zhang, H. Copper(I) Phosphide Nanocrystals for In Situ Self-Generation Magnetic Resonance Imaging-Guided Photothermal-Enhanced Chemodynamic Synergetic Therapy Resisting Deep-Seated Tumor. *Adv. Funct. Mater.* **2019**, *29* (50), 1904678.

(24) Tian, J.; Liu, Q.; Cheng, N.; Asiri, A. M.; Sun, X. Self-supported Cu_3P nanowire arrays as an integrated high-performance three-dimensional cathode for generating hydrogen from water. *Angew. Chem., Int. Ed.* **2014**, *53* (36), 9577−9581.

(25) Ma, L.; Shen, X.; Zhou, H.; Zhu, J.; Xi, C.; Ji, Z.; Kong, L. Synthesis of Cu_3P nanocubes and their excellent electrocatalytic efficiency for the hydrogen evolution reaction in acidic solution. *RSC Adv.* **2016**, *6* (12), 9672−9677.

(26) Wei, S.; Qi, K.; Jin, Z.; Cao, J.; Zheng, W.; Chen, H.; Cui, X. One-Step Synthesis of a Self-Supported Copper Phosphide Nanobush for Overall Water Splitting. *ACS Omega* **2016**, *1* (6), 1367−1373.

(27) Lu, C.; Wang, J.; Czioska, S.; Dong, H.; Chen, Z. Hierarchically Structured Cu-Based Electrocatalysts with Nanowires Array for Water Splitting. *J. Phys. Chem. C* **2017**, *121* (46), 25875−25881.

(28) Pi, M.; Yang, T.; Wang, S.; Chen, S. One-pot synthesis of in situ carbon-decorated Cu_3P particles with enhanced electrocatalytic hydrogen evolution performance. *J. Mater. Res.* **2018**, *33* (5), 546−555.

(29) Wang, H.; Zhou, T.; Li, P.; Cao, Z.; Xi, W.; Zhao, Y.; Ding, Y. Self-Supported Hierarchical Nanostructured NiFe-LDH and Cu_3P Weaving Mesh Electrodes for Efficient Water Splitting. *ACS Sustainable Chem. Eng.* **2018**, *6* (1), 380−388.

(30) Shen, R.; Xie, J.; Ding, Y.; Liu, S.-y.; Adamski, A.; Chen, X.; Li, X. Carbon Nanotube-Supported Cu_3P as High-Efficiency and Low-Cost Cocatalysts for Exceptional Semiconductor-Free Photocatalytic H_2 Evolution. *ACS Sustainable Chem. Eng.* **2019**, *7* (3), 3243−3250.

(31) Wang, R.; Dong, X. Y.; Du, J.; Zhao, J. Y.; Zang, S. Q. MOF-Derived Bifunctional Cu_3P Nanoparticles Coated by a N,P-Codoped Carbon Shell for Hydrogen Evolution and Oxygen Reduction. *Adv. Mater.* **2018**, *30* (6), 1703711.

(32) Zheng, H.; Huang, X.; Gao, H.; Lu, G.; Dong, W.; Wang, G. Cu@Cu_3P Core-Shell Nanowires Attached to Nickel Foam as High-Performance Electrocatalysts for the Hydrogen Evolution Reaction. *Chem. Eur. J.* **2018**, *25* (4), 1083−1089.

(33) Sun, W.; Fu, Z.; Shi, H.; Jin, C.; Liu, E.; Zhang, X.; Fan, J. Cu_3P and Ni_2P co-modified $g-C_3N_4$ nanosheet with excellent photocatalytic H_2 evolution activities. *J. Chem. Technol. Biotechnol.* **2020**, *95* (12), 3117−3125.

(34) Dutta, A.; Dutta, S. K.; Mehetor, S. K.; Mondal, I.; Pal, U.; Pradhan, N. Oriented Attachments and Formation of Ring-on-Disk Heterostructure Au−Cu_3P Photocatalysts. *Chem. Mater.* **2016**, *28* (6), 1872−1878.

(35) Dutta, A.; Samantara, A. K.; Adhikari, S. D.; Jena, B. K.; Pradhan, N. Au Nanowire-Striped Cu_3P Platelet Photoelectrocatalysts. *J. Phys. Chem. Lett.* **2016**, *7* (6), 1077−1082.

(36) Sun, Z.; Yue, Q.; Li, J.; Xu, J.; Zheng, H.; Du, P. Copper phosphide modified cadmium sulfide nanorods as a novel p−n heterojunction for highly efficient visible-light-driven hydrogen production in water. *J. Mater. Chem. A* **2015**, *3* (19), 10243−10247.

(37) Dutta, S. K.; Mehetor, S. K.; Pradhan, N. Metal Semiconductor Heterostructures for Photocatalytic Conversion of Light Energy. *J. Phys. Chem. Lett.* **2015**, *6* (6), 936−944.

(38) Tan, S.; Argondizzo, A.; Ren, J.; Liu, L.; Zhao, J.; Petek, H. Plasmonic coupling at a metal/semiconductor interface. *Nat. Photonics* **2017**, *11* (12), 806−812.

(39) Wang, Y.; Wang, Q.; Zhan, X.; Wang, F.; Safdar, M.; He, J. Visible light driven type II heterostructures and their enhanced photocatalysis properties: a review. *Nanoscale* **2013**, *5* (18), 8326−8339.

(40) Low, J.; Yu, J.; Jaroniec, M.; Wageh, S.; Al-Ghamdi, A. A. Heterojunction Photocatalysts. *Adv. Mater.* **2017**, *29* (20), 1601694.

(41) Bai, S.; Jiang, W.; Li, Z.; Xiong, Y. Surface and Interface Engineering in Photocatalysis. *ChemNanoMat* **2015**, *1* (4), 223−239.

(42) Bai, S.; Xiong, Y. Some recent developments in surface and interface design for photocatalytic and electrocatalytic hybrid structures. *Chem. Commun.* **2015**, *51* (51), 10261−10271.

(43) Bai, S.; Wang, L.; Li, Z.; Xiong, Y. Facet-Engineered Surface and Interface Design of Photocatalytic Materials. *Adv. Sci.* **2017**, *4* (1), 1600216.

(44) Xie, X.; Shen, W. Morphology control of cobalt oxide nanocrystals for promoting their catalytic performance. *Nanoscale* **2009**, *1* (1), 50−60.

(45) Liu, G.; Yu, J. C.; Lu, G. Q.; Cheng, H. M. Crystal facet engineering of semiconductor photocatalysts: motivations, advances and unique properties. *Chem. Commun.* **2011**, *47* (24), 6763−6783.

(46) Zhou, K.; Li, Y. Catalysis based on nanocrystals with well-defined facets. *Angew. Chem., Int. Ed.* **2012**, *51* (3), 602−613.

(47) Li, R.; Zhang, F.; Wang, D.; Yang, J.; Li, M.; Zhu, J.; Zhou, X.; Han, H.; Li, C. Spatial separation of photogenerated electrons and holes among {010} and {110} crystal facets of BiVO₄. *Nat. Commun.* **2013**, *4* (1), 1432.

(48) Butburee, T.; Kotchasarn, P.; Hirunsit, P.; Sun, Z.; Tang, Q.; Khemthong, P.; Sangkhun, W.; Thongsuwan, W.; Kumnorkaew, P.; Wang, H.; Faungnawakij, K. New understanding of crystal control and facet selectivity of titanium dioxide ruling photocatalytic performance. *J. Mater. Chem. A* **2019**, *7* (14), 8156−8166.

(49) Su, Y.; Li, H.; Ma, H.; Robertson, J.; Nathan, A. Controlling Surface Termination and Facet Orientation in Cu₂O Nanoparticles for High Photocatalytic Activity: A Combined Experimental and Density Functional Theory Study. *ACS Appl. Mater. Interfaces* **2017**, *9* (9), 8100−8106.

(50) Wang, L.; Ge, J.; Wang, A.; Deng, M.; Wang, X.; Bai, S.; Li, R.; Jiang, J.; Zhang, Q.; Luo, Y.; Xiong, Y. Designing p-type semiconductor-metal hybrid structures for improved photocatalysis. *Angew. Chem., Int. Ed.* **2014**, *53* (20), 5107−5111.

(51) Bai, S.; Li, X.; Kong, Q.; Long, R.; Wang, C.; Jiang, J.; Xiong, Y. Toward Enhanced Photocatalytic Oxygen Evolution: Synergetic Utilization of Plasmonic Effect and Schottky Junction via Interfacing Facet Selection. *Adv. Mater.* **2015**, *27* (22), 3444−3452.

(52) Du, J. S.; Chen, P. C.; Meckes, B.; Xie, Z.; Zhu, J.; Liu, Y.; Dravid, V. P.; Mirkin, C. A. The Structural Fate of Individual Multicomponent Metal-Oxide Nanoparticles in Polymer Nanoreactors. *Angew. Chem., Int. Ed.* **2017**, *56* (26), 7625−7629.

(53) Chen, P. C.; Liu, M.; Du, J. S.; Meckes, B.; Wang, S.; Lin, H.; Dravid, V. P.; Wolverton, C.; Mirkin, C. A. Interface and heterostructure design in polyelemental nanoparticles. *Science* **2019**, *363* (6430), 959−964.

(54) Huang, L.; Lin, H.; Zheng, C. Y.; Kluender, E. J.; Golnabi, R.; Shen, B.; Mirkin, C. A. Multimetallic High-Index Faceted Heterostructured Nanoparticles. *J. Am. Chem. Soc.* **2020**, *142* (10), 4570−4575.

(55) Snellman, M.; Eom, N.; Ek, M.; Messing, M. E.; Deppert, K. Continuous gas-phase synthesis of core−shell nanoparticles via surface segregation. *Nanoscale Adv.* **2021**, *3* (11), 3041−3052.

(56) Tang, L.; Wu, W.; He, L.; Yu, K.; Xu, T.; Zhang, Q.; Zhang, L.; Sun, L. Novel Interface in CuAg Nanostructure Induced by Size Effect. *J. Phys. Chem. Lett.* **2019**, *10* (8), 1973−1980.

(57) Suh, I.-K.; Ohta, H.; Waseda, Y. High-temperature thermal expansion of six metallic elements measured by dilatation method and X-ray diffraction. *J. Mater. Sci.* **1988**, *23* (2), 757−760.

(58) Wooten, A. J.; Werder, D. J.; Williams, D. J.; Casson, J. L.; Hollingsworth, J. A. Solution-liquid-solid growth of ternary Cu-In-Se semiconductor nanowires from multiple- and single-source precursors. *J. Am. Chem. Soc.* **2009**, *131* (44), 16177−16188.

(59) Subramanian, P. R.; Perepezko, J. H. The Ag-Cu (Silver-Copper) System. *J. Phase Equilib.* **1993**, *14* (1), 62−75.

(60) De Trizio, L.; Figuerola, A.; Manna, L.; Genovese, A.; George, C.; Brescia, R.; Saghi, Z.; Simonutti, R.; Van Huis, M.; Falqui, A. Size-Tunable, Hexagonal Plate-like Cu₃P and Janus-like Cu-Cu₃P Nanocrystals. *ACS Nano* **2012**, *6* (1), 32−41.

(61) Kubashewski, O.; Semenova, E. L. Ag-Cu-P (Silver-Copper-Phosphorus). In *Non-Ferrous Metal Systems. Part 3*; Effenberg, G., Ilyenko, S., Eds.; Springer-Verlag Berlin Heidelberg, 2007; pp 38−46.

(62) Lyu, Z.; Chen, R.; Mavrikakis, M.; Xia, Y. Physical Transformations of Noble-Metal Nanocrystals upon Thermal Activation. *Acc. Chem. Res.* **2021**, *54* (1), 1−10.

(63) Coene, W. M. J.; Thust, A.; Op de Beeck, M.; Van Dyck, D. Maximum-likelihood method for focus-variation image reconstruction in high resolution transmission electron microscopy. *Ultramicroscopy* **1996**, *64* (1−4), 109−135.

(64) Hÿtch, M. J.; Snoeck, E.; Kilaas, R. Quantitative measurement of displacement and strain fields from HREM micrographs. *Ultramicroscopy* **1998**, *74* (3), 131−146.

(65) Bhattarai, N.; Casillas, G.; Ponce, A.; Jose-Yacaman, M. Strain-release mechanisms in bimetallic core-shell nanoparticles as revealed by Cs-corrected STEM. *Surf. Sci.* **2013**, *609*, 161−166.

(66) García-Negrete, C. A.; Knappett, B. R.; Schmidt, F. P.; Rojas, T. C.; Wheatley, A. E. H.; Hofer, F.; Fernández, A. Island-type growth of Au−Pt heterodimers: direct visualization of misfit dislocations and strain-relief mechanisms. *RSC Adv.* **2015**, *5* (68), 55262−55268.

(67) Meyer, J. C.; Girit, C. O.; Crommie, M. F.; Zettl, A. Hydrocarbon lithography on graphene membranes. *Appl. Phys. Lett.* **2008**, *92* (12), 123110.

(68) Hetherington, C.; Jacobsson, D.; Dick, K. A.; Wallenberg, L. R. In situ metal-organic chemical vapour deposition growth of III−V semiconductor nanowires in the Lund environmental transmission electron microscope. *Semicond. Sci. Technol.* **2020**, *35* (3), 034004.